A Single Molecule View of Conformational Switching of DNA Tethered to a Gold Electrode

By: Eric A. Josephs and Tao Ye

Josephs, E. A. and T. Ye. "A Single Molecule View of Conformational Switching of DNA Tethered to a Gold Electrode." *Journal of the American Chemical Society,* **2012**, *134* (24), 10021– 10030. https://doi.org/10.1021/ja3010946

Abstract:

Surfaces that can actively regulate binding affinities or catalytic properties in response to external stimuli are a powerful means to probe and control the dynamic interactions between the cell and its microenvironment. Active surfaces also enable novel functionalities in biosensors and biomolecular separation technologies. Although electrical stimuli are often appealing due to their speed and localization, the operation of these electrically activated surfaces has mostly been characterized with techniques averaging over many molecules. Without a molecular-scale understanding of how biomolecules respond to electric fields, achieving the ultimate detection sensitivity or localized biological perturbation with the ultimate resolution would be difficult. Using electrochemical atomic force microscopy, we are able to follow the conformational changes of individual, short DNA molecules tethered to a gold electrode in response to an applied potential. Our study reveals conformations and dynamics that are difficult to infer from ensemble measurements: defects in the self-assembled monolayer (SAM) significantly perturb conformations and adsorption/desorption kinetics of surface-tethered DNA; on the other hand, the SAM may be actively molded by the DNA at different potentials. These results underscore the importance of characterizing the systems at the relevant length scale in the development of electrically switchable biofunctional surfaces.

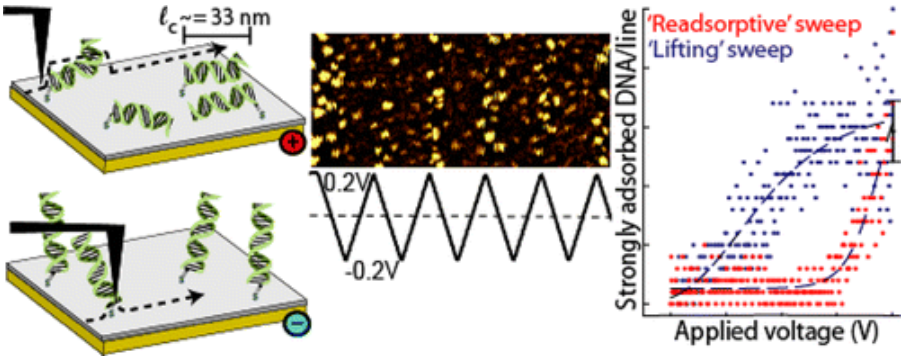

Keywords: DNA | self-assembled monolayer | atomic force microscopy | particle-counting voltammogram | biofunctional surfaces

Article:

Introduction

As static surfaces that can controllably interact with biomolecules become established, increasing attention has been paid to active biofunctional surfaces whose binding affinity or catalytic activity can be dynamically switched.[1, 2] The dynamic nature imparts novel functionalities that may be exploited for more sophisticated biosensors,[3-5] cell culture substrates,[2, 6] or self-assembled nanostructures.[7] A variety of triggers, such as light,[8, 9] pH,[10] temperature,[11] electrode potential,[12-14] and mechanical forces,[15] have been used to control surface properties on-demand. The application of electric fields provides an especially powerful route in the operation of these systems as electronic signals can be rapid and localized to within a few nanometers from the electrode surface,[16] and many biomolecules possess a net charge which may be acted upon by the field. Yet despite the inherent nanometer scale of both the (bio)molecular structures and their interactions on the surface, in general the operation of switchable surfaces has been characterized using ensemble measurements that provide limited structural information.[6, 13, 17] Nanoscale surface morphology and local distributions in the electric field strength are expected to impact the performance of a range of biosensors and may become even more important in ultrasensitive detection schemes or nanopatterns used to perturb cells.[1] Here we report that the conformational changes of DNA molecules tethered to a self-assembled monolayer (SAM) modified gold electrode can be probed at the single-molecule level with electrochemical atomic force microscopy (AFM). We were able to extract heretofore obscured details about how the local chemical environment on the surface affects the response of individual molecules to the applied potentials under conditions similar to those used to detect nucleic acids.[3]

Our model system, a thiolated oligonucleotide tethered to gold within a background hydroxyl-terminated alkanethiol SAM (Figure 1), is ubiquitous in both static[18-20] and dynamic[3-5] nucleic acids sensors. The SAM is needed to separate the probe molecules from each other as well as from the surface, as steric crowding and surface interactions impede hybridization.[18] Under an electrolyte, the metal surface is positively charged when the potential is above the potential of zero charge (pzc, ca. 100 mV vs Ag/AgCl for 6-mercapto-1-hexanol (MCH) on Au(111))[21] and negatively charged when below. The response of DNA, an anionic polyelectrolyte, to interfacial charges has been exploited to modulate hybridization or melting rates on microarrays and other nucleic acid sensing methods,[22-27] as well as to facilitate G-quadruplex formation.[28] Rant et al.[12, 17] have demonstrated a reversible orientational switching in response to applied potential using distance-dependent fluorescence quenching on gold; the surface-tethered DNA molecules tethered are lifted off MCH SAM at negative potentials, and attracted to a positively charged surface (Figure 1B,C). The orientational switching has been applied in label-free protein and nucleic acid detection.[3-5]

It was noted that the orientational switching is highly sensitive to sample preparation history.[12, 29] For example, controlled desorption of immobilized DNA, which was proposed to reduce the aggregation of adsorbed probe molecules, was required to activate switching. A recent fluorescence microscopy study of DNA orientational switching revealed heterogeneity even at the micrometer scale.[30] Although light microscopy does not have sufficient resolution to pinpoint the molecular-scale origin of this phenomenon, the study nevertheless showed that

complex molecular conformations or interactions with heterogeneous chemical environments, which directly impact the performance of the sensors, are difficult to infer from the limited information obtained, such as average density, layer thickness and orientation.[17, 19, 24, 31-33]

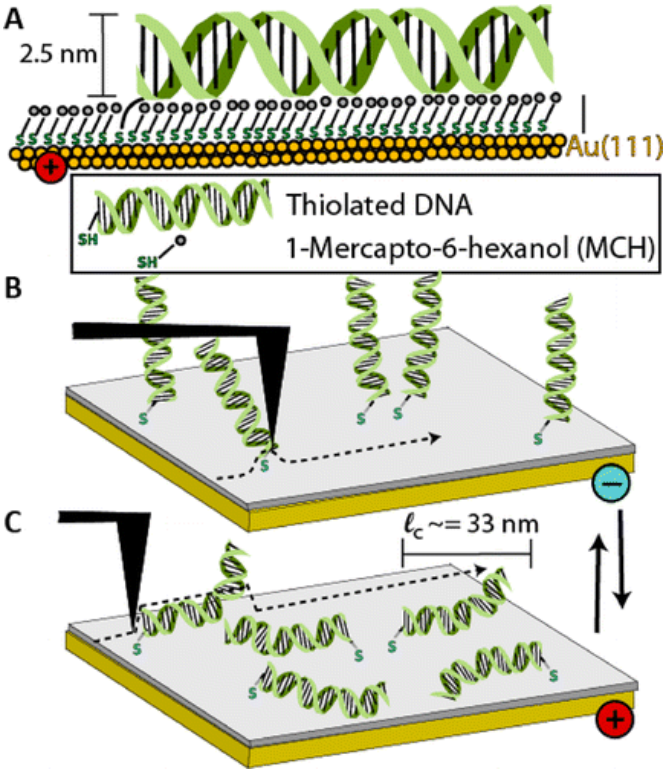

Figure 1. Schematic of an electrically switchable DNA monolayer (A) Thiolated 105bp DNA is covalently attached to an Au(111) electrode atop an alkanethiol monolayer. (B) At a negative potential, the tethered, negatively charged DNA is electrostatically lifted off the surface, making it too mobile to resolve clearly. (C) Application of a positive potential pins the DNA to the surface, limiting DNA mobility on the surface and allowing accurate measurement of the topographical heights by AFM.

Among the high-resolution scanning probe microscopy techniques, scanning tunneling microscopy (STM), which has been used to image DNA adsorbed on bare metal surfaces,[34-36] annot resolve DNA molecules adsorbed on top a SAM due to the poor conductivity. Currently AFM does not have sufficient resolution to resolve individual, fluctuating DNA molecules in a dense layer.[37] On the other hand, while success has been reported in resolving single-molecule features in low surface density DNA monolayer in air with AFM,[38] imaging individual DNA molecules tethered to sensor surfaces under aqueous solutions is complicated by the significantly increased mobility of the molecules.[39, 40] Resolving the switching presents an additional challenge because AFM scanning may be too slow (generally minutes per frame) to resolve the dynamic processes. An AFM force-spectroscopy study by Erdmann et al.[41] gained valuable insights into the potential-dependent interactions between individual DNA molecules and an SAM. Although force spectroscopy mapping in principle should provide spatial distribution of the interactions, such mapping is very slow and has poor lateral resolution.[42] Therefore, important questions concerning how to probe these dynamic structures with nanometer-resolution and how the interactions vary with local environments remained unaddressed.

Employing a series of strategies, including using a well-defined single-crystal surface, tailoring the nanoscale interactions between DNA and the SAM, and novel potentiodynamic AFM analysis to obtain the intraframe activity of the DNA, we have unraveled at the single-molecule level some of the complex molecular conformations and dynamics: defects in the passivating SAM significantly perturb DNA conformations. Strong interactions with the defects hinder orientational switching. The importance of defects on the switching behavior may be a consequence of their ability to concentrate strong local electric fields, the exposure of alkyl chains that have hydrophobic interactions with the nucleobases, as well as opportunities for the DNA to adhere directly to the gold substrate. In addition, our study shows that the MCH SAM cannot be treated as a static surface, as commonly assumed. The SAM may be actively molded by the DNA at certain potentials. These results highlight the many ways dynamic nanoscale surfaces differ from their static counterparts and underscore the importance of characterizing the systems at the relevant length scale in the development of electrically switchable biofunctional surfaces.

Experimental Methods

Materials

Gold wire (99.99%, 1 mm diameter) was purchased from Scientific Instrument Services, Inc. 6-Mercapto-1- hexanol (MCH) was purchased from Santa Cruz Biotechnology, Inc. Tris-acetate-EDTA (TAE), 10× solution, and dithiothreitol (DTT), 99%, were purchased from Fisher Scientific. The synthetic oligonucleotides were purchased from IDT Technologies and used without further purification. Only ultrapure water (>18 MΩ·cm) generated from a Barnstead Diamond Nanopure water purification system was used.

Preparation of the Gold Surface

For AFM experiments, a gold bead containing single-crystal facets was made by melting a gold wire in the manner of Clavilier et al.[43] and then mounted on a platinum foil. For cyclic voltammetry, an Au(111) disk (MaTeck, Gemany) was used instead.

Preparation of the Thiolated DNA

First, 105 bp (short) and 503 bp (long) double-stranded DNA molecules which contained a thiol group connected by a hexyl chain (a “thiol tether”) to the 5′-end of one of the DNA strands were prepared by PCR using OneTaq kit (New England Biolabs). M13mp18 RF I DNA (New England Biolabs) was used as the substrate and oligos A and B or oligos A and C were used as primers for the 105 bp DNA or the 503 bp DNA, respectively:

Oligo A: 5′-/5ThioMC6-D/TTT TTG ACC AACTTT GAA AGA GGA CAG ATG AAC GG-3′
Oligo B: 5′-AAT GAA TAT CCG GTT CTT GTC AAG ATT ACT C-3′
Oligo C: 5′-CCC TCT GGC AAA ACT TCT TTT GCA AAA GC-3′

where /ThioMC6-D/is the thiol tether. The product was purified via agarose gel electrophoresis and Qiagen Gel Purification kit. Next, 50 μL of the purified PCR product was mixed with 15 μL

of 1 M reducing agent DTT in Tris-EDTA buffer under nitrogen for >1 h, then washed using a illustra NAP-5 column (GE Healthcare) and re-eluted in 1× Tris-acetate-EDTA solution (40 mM Tris-acetate, 1 mM EDTA) to a final concentration of 5 nM. DNA was stored in aliquots at −20 or −80 °C (long-term) until prior to assembly on surface.

Switchable Monolayer Assembly

The gold substrate was cleaned in hot nitric acid then annealed with an H_2 flame immediately prior to immersion in the alkanethiol solution of 1:1 (by volume) 1×TAE:ethanol containing a few drops of neat MCH (10–100 mM) under a nitrogen atmosphere. The bead was left overnight or up to a few days in the solution, rinsed with 1×TAE, and then immersed into a shallow beaker containing 5 nM solution of 503 bp DNA or 100× diluted 105 bp DNA for 1–5 min (the "insertion" method—see Results and Discussion). The beads were rinsed copiously with 10× concentrated TAE solution (400 mM Tris-acetate, 10 mM EDTA) to reduce nonspecific adsorption, dried with a stream of filtered air, then loaded immediately into the AFM liquid cell.

In Situ Electrochemical AFM

AFM (Agilent 5500) was performed by tapping-mode imaging in aqueous 0.5×TAE solution (20 mM Tris-acetate, 0.5 mM EDTA) using a custom-built fluid cell. Within the fluid cell we placed a Pt/Ir wire that was used as a counter electrode and a small Ag/AgCl reference electrode, which has a low leakage junction formed by the gap between a Pt wire and glass. SNL-10 (Bruker) probes were used for all experiments; the shorter two of the four cantilevers (spring constants of approximately 0.2–0.4 N/m) were used. The counter and reference electrodes as well as the fluid cell itself were cleaned in piranha solution (1:3 H_2O_2: H_2SO_4) prior to use and copiously rinsed with water. ***CAUTION:*** *Piranha solution can react violently with organic materials, and should be handled with personal protective equipment. Piranha solution should not be stored in tightly sealed containers.* For experiments under N_2, AFM was performed in an environmental chamber. N_2 was purged into the chamber for several minutes prior to and during imaging, and N_2 bubbled into the 0.5× TAE solution for several minutes prior to use; no qualitative difference was found between these experiments and those performed without the environmental chamber. A potential was applied to the surface (the gold bead used as the working electrode) from the integrated potentiostat in the AFM controller. During imaging, topographical, amplitude, and phase channels were recorded as well as applied potential and current. Imaging was generally performed with a scan rate of 1–1.5 lines/s at 512 pixels/line.

Results and Discussion

A dilute monolayer of DNA supported by an alkanethiol background was prepared by the "insertion" method,[30, 44] in which a pre-formed alkanethiol monolayer was exposed to thiolated DNA. Isolated protrusions 0.50 ± 0.14 nm high appeared in the AFM image at the open-circuit potential, −80 mV vs Ag/AgCl (Figure 2A,C, and Table 1). The protrusions suggest that the insertion approach we adopted produces DNA molecules separated from each other. The isolation of molecules likely resulted from preferential adsorption of DNA into SAM defects and the electrostatic repulsion between the DNA molecules.[45, 46] In addition, insertion is known be more effective in preserving the order of the host SAM structure than other coadsorption

methods.[44] A fluorescence spectroscopy and microscopy study showed that the monolayer prepared with this method displayed more consistent switching behavior and notably reduced heterogeneity.[30] The well-defined DNA/SAM surface with minimal aggregation not only facilitates single-molecule studies but also should allow more efficient hybridization and predictable orientation switching on sensor surfaces.

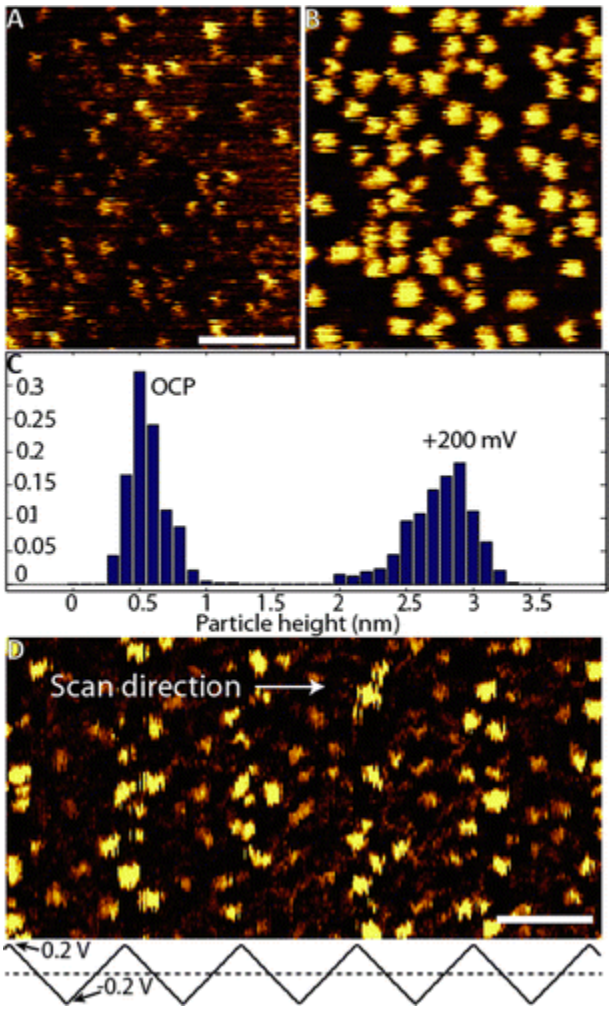

Figure 2. Tapping-mode AFM images of thiolated 105bp DNA on an MCH background at different electrochemical potentials. Scale bars are 100 nm. (A) At open-circuit potential (OCP ≈ −80 mV vs Ag/AgCl), only 0.5 nm high protrusions, attributed to the anchor point, were observed. (B) At +200 mV, protrusions approximately 2.7 nm tall, close to the diameter of dsDNA, were visible. (C) Height histograms of protrusions at OCP and +200 mV. (D) While cycling the potential between +200 and −200 mV at 25 mV/s, the AFM probe rasters vertically and proceeds from left to right at 1.5 lines/s. The DNA molecules alternate discretely between the two heights as a function of the potential (below).

After the potential was increased to +600 mV (Figure S1), a potential which we have verified does not significantly desorb the monolayer through oxidation[47] (Figures S2 and S3, and see below) of alkanethiols, well-defined protrusions appeared. These protrusions persisted even when the potential was reduced to +200 mV (Figure 2B,C, and Table 1). The height, 2.74 ± 0.25

nm, close to the diameter of double-stranded DNA, suggests that the molecules were pinned down onto the SAM by positive surface charges. Even when immobilized, the 105 bp (contour length $l_c \approx 33$ nm) DNA appears globular instead of rod-like under AFM. Similar morphology has been observed for short oligonucleotides immobilized on mica[40] and can be attributed to the residual conformational fluctuation of the immobilized DNA and the tip convolution effect, which may broaden the feature by 17 nm assuming a tip radius of curvature of 15 nm. It may appear counterintuitive that while the molecules may stand up at negative potentials, they do not appear as high as molecules lying down at +200 mV under AFM. The apparent contradiction can be readily explained by the contrast mechanism of tapping-mode AFM: in order for a structure to be resolved, it must remain immobile during the time scale at which the tip traverses over the molecule.[48] Structures that move rapidly in and out of the tip–surface junction, such as the solvent molecules, are not imaged. The morphology at −80 mV suggests that only segments close to the tethers were resolved due to reduced mobility (as in Figure 1B,C). No DNA molecules could be observed during a control experiment where a pre-formed MCH SAM had been exposed for 2 h to a solution containing unthiolated DNA, which were likely washed away during rinsing (Figure S4).

Table 1. Assignment of Orientations and Adsorption Sites of DNA According to Apparent Heights

			calculated height/nm		
Figure	**system**	**SAM thickness/nm**	**DNA lying down on SAM**	**DNA lying down on Au**	**apparent height[a]/nm**
2A	105 bp DNA/MCH	1.0	2.5	1.5	0.50 ± 0.14
2B					2.74 ± 0.25
5B	503 bp DNA/MCH	1.0	2.5	1.5	3.63 ± 0.62
5D					1.54 ± 0.35

[a] The heights of the molecules are referenced to the top of the background SAM. Because the diameter of double-stranded DNA and the thickness of the SAM are known, the apparent heights can be compared to the calculated heights of DNA in different adsorption configuration.

The protrusions switched reversibly between the two morphologies when the potential was cycled between +200 and −200 mV (Figures 2D and S5). A question arises whether the changes in the apparent height in Figure 2 could be attributed to imaging artifacts due to potential-dependent change in double-layer forces. Barton et al.[37] have convincingly argued that the contribution is rather minor for DNA tethered to an electrode surface. First, the change in the double-layer force is at most 10 pN, much smaller than the nN peak force exerted by the tapping-mode AFM. We found the morphology to be insensitive to the tapping amplitude set-point. Second, the double-layer force is a continuous, approximately linear function of the electrode potential.[16] However, we find the DNA switch discretely between the amorphous and taller/globular features: the transition from the amorphous features to taller protrusions occurs over just 100 mV when the potential is swept from −200 to +200 mV; and the heights of the taller features at +200 mV are approximately the same as those at +600 mV (Figure S6). Third, the time scale of change in the double-layer force is related to the RC (double-layer charging) time constant, on the order of milliseconds.[49] Therefore, any change due to the double-layer force should be almost instantaneous under AFM. However, the potentiodynamic images in Figure 2D displayed a hysteresis between the potential where the DNA become taller/globular ("strongly immobilized") and the potential where the features are amorphous ("lifted") (see

below), which indicates that the time scale of these processes is on the order of seconds. Therefore, we conclude that the change in morphology originated from molecular scale structural changes instead of an imaging artifact due to contrast changes when the potential is varied.

Although the tethered DNA molecules are found to lie down on the surface at positive potentials using fluorescence spectroscopy,[12] they were not clearly resolved by AFM until a potential of +600 mV was first applied, and cycling between +200 and −200 mV did not result in the switching of morphology if +600 mV was not first applied (Figure S1). The strong immobilization after the treatment at +600 mV indicates that there are some permanent structural changes to the SAM. We propose that small defects in the SAM immobilize DNA molecules. Neither significant defects in the SAM nor apparent heights of DNA noticeably lower than 2.5 nm after the treatment were observed in Figure 2; this suggests that the treatment produced pinhole defects smaller than 2.5 nm. Defects larger than the diameter of the DNA are expected to reduce the apparent height of the adsorbed DNA to below 2.5 nm. Because the height of the DNA immobilized at positive potentials is measured relative to the background substrate, it is possible that MCH monolayer and thiol tethers of the DNA are oxidatively desorbed at +600 mV and the features we observe are DNA lying directly atop the gold as in ref 34. However, this possibility is inconsistent with results from several experiments that probe the stability of the SAM. The capacitance of the MCH monolayer held at +600 mV under 0.5×TAE increased modestly, from 2.5 to 3.1 μF/cm^2 over 25 min (Figure S2); had the monolayer been entirely oxidized, we would expect a capacitance that was at least 10-fold larger.[50] This result suggests that the surface coverage of MCH remain close to a full monolayer and the surface coverage of defects induced at +600 mV is small. If we intentionally exposed the surface to harsh electrochemical conditions (rapid cycling between 0 and +800 mV), we could resolve a dramatic increase in monolayer roughness by AFM (Figure S3). Therefore, +600 mV remains below the potential range that leads to significant oxidative desorption at the experimental time scale.

Additionally, the protrusions observed in Figure 2 underwent no significant lateral motion even after multiple potential cycles. “Lifted” molecules can be observed at the precise location where a “strongly immobilized” molecule had been previously observed at +200 mV, on a one-to-one basis (Figure S7). This strongly implies that not only are the DNA molecules lifting and rotating about their thiol tethers in response to the applied potentials, but that the MCH monolayer is largely stable and capable of serving as a barrier to surface diffusion of the DNA molecules. Because the Au–S bond is known to be labile at room temperature, individual alkanethiol molecules on gold surfaces at low coverages diffuse rapidly and cannot be resolved by AFM or STM until they are confined in crystalline structures[51] or cooled down to cryogenic temperatures.[52] Had the MCH monolayer oxidatively desorbed, the lifted DNA molecules, with only the thiol tether in contact with the surface, would have been unlikely to be observable under AFM. Rather, we propose that pinhole defects are formed near DNA molecules within a mostly crystalline SAM at +600 mV. The exact mechanism of defect formation remains unclear: the defects could result from a small amount of desorption; the defects may be directly formed through an interaction with the electric field in a phenomenon similar to electroporation,[53] in which small pores in lipid membranes open up in response to the strong fields applied across the membranes; alternatively, the DNA, attracted by the positive surface charges, may exert a local pressure that disrupts the SAM, especially at the tether point. Such a disruption would concentrate the electric field and further allow the DNA to be “pinned” to the surface for

imaging at positive potentials, while leaving the majority of the monolayer intact. Clear evidence of the SAM disruption directly induced by DNA can be found in our investigations of MCH monolayers with longer DNA molecules in Figures 5 and 7, below. An *in situ* STM study of the MCH SAM may be needed to elucidate the origin and the structure of the defects. It should be pointed out that the treatment at +600 mV may not even be necessary for defect-mediated conformational switching of DNA on the rougher polycrystalline gold substrates often used as biosensor surfaces, as SAM defects on these surfaces are more abundant.[54] As achieving unambiguous, molecular resolution on the polycrystalline surfaces with AFM is difficult, the MCH SAM on a single-crystal Au(111) surface, with controllably introduced defects, can serve as a model system to understand DNA–electrode interactions on realistic biosensor surfaces at the molecular level.

The presence of a defect near a DNA molecule is expected to dramatically affect the local electric field distribution to which the molecule is subjected. The diffuse layer potential ψ_D (V) above a perfectly crystalline alkanethiol monolayer at electrode potential V can be found under conditions of charge balance (assuming no charges on the alkanethiol tail-groups) in eq 1 between the metal surface and the surface of the monolayer and by treating the monolayer as an ideal capacitor in eq 2.[16, 55]

$$\sigma_{\mathrm{m}} = \sigma_{\mathrm{s}} \tag{1}$$

σ_m is the charge density of the metal surface:

$$\sigma_{\mathrm{m}} = \frac{\varepsilon_0 \varepsilon_{\mathrm{r,m}}}{d}\left(V - V_{\mathrm{pxc}} - \psi_{\mathrm{D}}\right) \tag{2}$$

where ε_0, $\varepsilon_{r,m}$, d, and V_{pzc} are the vacuum permittivity, the relative permittivity of the monolayer (2.25), the thickness of the monolayer (1.02 nm), and the pzc. The surface charge density σ_s of the monolayer can be determined by the Grahame equation (eq 3) and eq 4 for n species of electrolytes with charge z.[56]

$$\sigma_{\mathrm{s}} = \sqrt{2\varepsilon_0 \varepsilon_{\mathrm{s}} k_{\mathrm{B}} T \left(\sum_i^n c_{0i} - \sum_i^n c_{\infty i}\right)} \tag{3}$$

$$c_{0i} = c_{\infty i} \exp\left(-z_i \beta \psi_{\mathrm{D}}\right) \tag{4}$$

where ε_s, k_BT, β, and $c_{\infty i}$ are the relative permittivity of the electrolyte solution, the thermal energy, the reciprocal of thermal energy, and the bulk number density of electrolyte species i, respectively. The diffuse layer potential can then be found numerically. At 200 mV above pzc in 0.5×TAE (with Debye length $\kappa = 2.7$ nm), the MCH monolayer has $\psi_D \approx 15$ mV. Under these moderate potentials, the Debye–Hückel approximation can be used to estimate the potential in the solution, and the electric field near the interface has a maximum value of $\psi_D\kappa^{-1} = 5.6$ MV/m. To obtain an estimate of the electric field strength at a monolayer defect, we numerically solved

a modified Poisson–Boltzmann equation (eqs 5 and 6), which takes into account the size of ions in confined spaces (Figure S8).[57]

$$\varepsilon_0 \varepsilon_s \nabla^2 \psi = \frac{8\pi e c_b \sinh(\beta e \psi)}{1 - \varphi_0 + \varphi_0 \cosh(\beta e \psi)} \quad (5)$$

$$\varphi_0 = 2a^3 c_b \quad (6)$$

where a is the size of the ionic species. Within a 2 nm wide defect we find the electric field has a maximum strength of 50–60 MV/m, an order of magnitude larger than above a pristine monolayer. While the potential drop in an ordered monolayer decreases the diffuse layer potential and electric field, defect sites are able to maintain higher electric fields. Although more sophisticated molecular-scale simulations of SAM defect sites may be needed to account for solvation within the hydrophobic defect[58] and obtain a more accurate electric field distribution, our estimate nevertheless showed that the stronger electrostatic interactions within the defects may sufficiently hinder rotational diffusion of the tethered molecules and "trap" the DNA at the surface, allowing for clear resolution by AFM.

To quantify the kinetic response of the DNA to the applied electrode potentials we examined the potentiodynamic image obtained during simultaneous imaging and potential sweep (Figure 2D). Analysis of dynamic processes using AFM is often based on frame-by-frame examination of changes to features on the surface,[59, 60] which in our case would limit the temporal resolution to minutes. Because the DNA molecules on the surface are individually resolvable, isolated, and isotropically distributed—but sufficiently dense—we were able to study the switching kinetics with a higher time resolution (seconds) by constructing what we termed a particle-counting voltammogram (PCV) from intraframe data. In a PCV experiment, the potential applied to an electrode $V(t)$ is linearly swept from an initial voltage V_0 at rate λ during imaging by AFM. The number of strongly adsorbed molecules (taller/globular with height >1.5 nm, see Figure 2C) observed during a single line scanned by the AFM is then determined for that given applied potential. As an AFM records images by rastering serially (line by line) across a surface, the slow scan axis also represents the time axis. While a PCV experiment does provide a means to probe processes that are too fast for frame by frame analysis, a consequence is that we cannot keep track of a specific molecule in different frames. Instead, we must (initially) assume that the behavior of the molecules imaged during a single scan line at the concurrent potential is indicative of the behavior of all of the molecules on the surface and interpret our data from an ensemble point of view assuming homogeneous kinetics. Later we examine the validity of this assumption with a kinetic Monte Carlo simulation[61] of the experiment.

In Figure 3A, the sweep of the PCV from +200 to −200 mV at 25 mV/s, during which DNA should "lift" from the strongly adsorbed state (blue), did not overlap with that of the "readsorption" sweep from −200 to +200 mV (red), which suggests that the transition to the mobile state is slow on the time scale of the sweep. This is in contrast to fluorescence spectroscopy studies showing that tethered DNA switched within milliseconds between a surface-bound state and a lifted state.[12, 17, 49] This discrepancy can be resolved if we invoke a weakly surface-bound state (W), which is oriented close to the surface but remains too mobile to be resolvable by AFM (Figure 4). From the PCV and existing fluorescence experimental data we

expect that the conversion between a strongly adsorbed state (A) and W is slow, but between W and a lifted state (L) conversion is rapid. Assuming a quasi-equilibrium between W and L (state W*), the time dependence of the fraction of molecules in the A state can be described by eq 7, in which $\hat{g}(V)$ is the potential-dependent Boltzmann factor describing the fraction of W among the combined population of W and L (SI), and θ_a and θ_T represent the surface coverages of strongly adsorbed DNA and all DNA species on the surface, respectively.

$$\frac{d\theta_a}{dt} = -k_d(V)\theta_a + k_a(V)\hat{g}(V)(\theta_T - \theta_a) \tag{7}$$

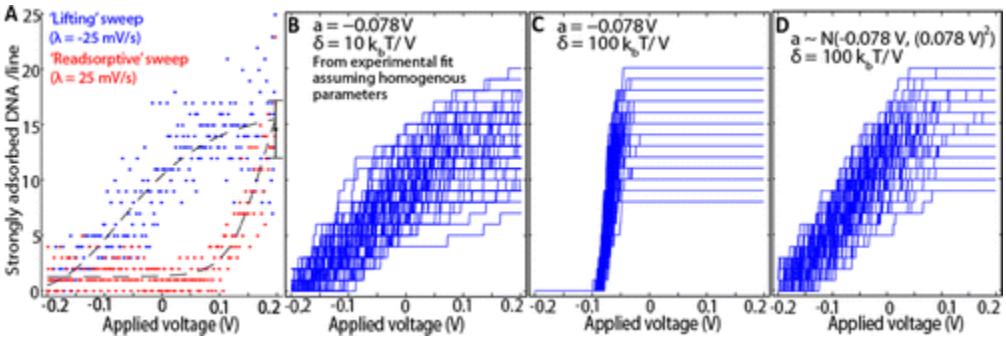

Figure 3. Particle counting voltammogram (PCV) from potentiodynamic AFM images. (A) PCV of the taller/globular ("strongly adsorbed") protrusions observed during a line scan versus the potential applied in Figure S5B (uncropped version of Figure 2D). Blue data points were observed while the potential was being swept in the negative direction (DNA "lifting") at sweep rate $\lambda = -25$ mV/s, while the red data points were taken during the positive direction sweep (DNA "readsorbing") at $\lambda = 25$ mV/s. Black data point and error bars are the mean and standard deviation of number of particles >1.5 nm tall observed/line at a constant potential of +200 mV. (B–D) Kinetic Monte Carlo simulations of the PCV data from the "lifting" sweep from +200 to −200 mV using parameters in the inset, with parameter δ as the voltage dependence of the activation barrier to lifting (see text) and parameter *a* approximately the mean voltage of DNA lifting, which is a function of the nonelectrostatic components of the lifting activation barrier. $N(\mu,\sigma^2)$ is a Gaussian random variable with mean μ and standard deviation σ. See SI for details.

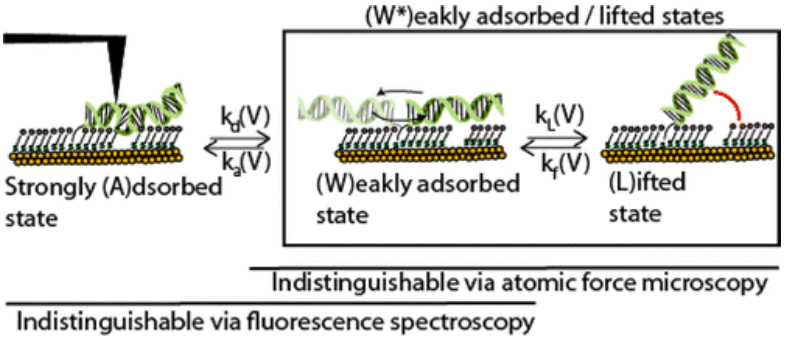

Figure 4. Proposed mechanism of DNA switching. DNA can only be imaged when in a "strongly adsorbed" state A, which is possibly a result of hydrophobic interactions between the grooves of the DNA and the alkanethiol defect sites, and appears as the taller/globular features with the AFM. The DNA may extract itself from its adsorption to the defects but remain weakly adsorbed to the surface through electrostatic interactions, gaining sufficient mobility as to no

longer appear as a globular feature (state W). The DNA can be further repelled away from the surface by electrostatic forces and be mostly decoupled from the surface except near its tether (state L). The rapidly equilibrated states W* appear as the amorphous features in AFM images.

We assume the voltage dependence of k_d and k_a can be described by a Butler–Volmer-like function (eq 8):

$$k(V) = \alpha\, \mathrm{e}^{-\delta V/\mathrm{k_B}T} \tag{8}$$

We justify this expression as follows: We assume the lifting of "strongly adsorbed" DNA behaves as an escape over an energy barrier ($\Delta G^{\ddagger}$, also referred to as the desorption activation energy) similar to that of a mechanical process subjected to a force F along its reaction coordinate.[62] k_d is defined as in eq 9, where ν is an Arrhenius-type prefactor and $\Delta x^{\ddagger}$ is the distance from the adsorbed state to the transition state along the reaction coordinate, which we assume remains approximately constant under the applied forces.[63]

$$k_{\mathrm{d}}(V) = \nu \mathrm{e}^{-(\Delta G^{\ddagger} + F\Delta x^{\ddagger})/k_{\mathrm{B}}T} \tag{9}$$

The force per unit length required to desorb a charged polymer on a charged surface (or electrode), which has been investigated theoretically[64] and demonstrated experimentally by single-molecule force spectroscopy,[41, 65] has been found to follow eq 10, where F_0 is the desorption force deriving from non-electrostatic terms (van der Waals forces, entropic forces, etc.), l_B is the Bjerrum length, τ is the line charge density of the polymer, $\sigma_s(V)$ is the surface charge density, and κ^{-1} is the Debye length of the solution.

$$F = F_0 + 4\pi k_{\mathrm{B}} \kappa^{-1} \tau l_{\mathrm{B}} \sigma_{\mathrm{s}}(V) \tag{10}$$

At moderate ionic strengths and low potentials, $\sigma_s(V)$ is a linear function of the applied potential, $\sigma_s(V) = (V - \mathrm{pzc})\varepsilon_0\varepsilon_r/d$ (SI), where d is the thickness of the SAM. Multiplying by the adsorbed length of the DNA and inserting this into eq 10 and then eq 9 yields the desired form of eq 8. A similar expression can be derived for k_a (as the escape "back over" the energy barrier). In eq 8, α is a pre-exponential factor that includes the attempt frequency as well as the non-electrostatic component of the activation energy, and δ represents the voltage dependence of the activation energy.

Extracting α and δ by fitting eq 7 to our experimental data is not yet possible given the uncertainty in Boltzmann factor $\hat{g}(V)$ in the differential equation. Nevertheless, we can estimate $\hat{g}(V)$ in a manner similar to Rant et al.[12] (SI) and observe that when $V <$ pzc, $\hat{g}(V)$ rapidly approaches 0. During the negative potential sweep ($\lambda < 0$) used for lifting of the DNA, we observe desorption when V decreases below 100 mV, and thus we can simplify our treatment of the desorption process as irreversible during the negative potential sweep; when a DNA molecule transitions from state A to state W* on a negative charged surface, there is a significant driving force to reorient the molecule away from the surface to minimize electrostatic repulsion. The transition from A to a mobile state (W*) is rather broad, occurring over 200 mV. By fitting the desorptive sweep of the PCV (blue) to eq 7 assuming negligible readsorption ($\hat{g}(V) = 0$), the apparent voltage dependence of the activation barrier is found to be about 1 k_BT/100 mV, which

appears small given the expected strong role of the electric field on desorption. An alternative explanation is that heterogeneous interactions experienced by adsorbed molecules in different chemical environments caused the molecules to desorb at different potentials. Similar effects have been observed in electrochemical kinetics, where a distribution of the standard rate constants of the electroactive molecules can lead to lower apparent charge transfer coefficient during a potential sweep experiment.[67, 68] A PCV experiment observing DNA with a distribution of the non-electrostatic term α could appear the same as a PCV measuring DNA with homogeneous adsorption energies and a weaker response of the lifting rate to an applied potential. To examine the effects of kinetic heterogeneity on the resulting PCV experiment, we performed a kinetic Monte Carlo (Figure 3B–D) simulation that takes into account the discrete nature of our molecular imaging. We were able to reproduce similar PCV results in both the case of DNA with homogeneous, weak sensitivity to the electric field (Figure 3B) and the case of DNA with a reasonably high sensitivity to the electric field (δ) but heterogeneous non-electrostatic components of the desorption activation energy (parameter *a*, which is approximately the mean potential of DNA lifting and a function of the non-electrostatic components to the desorption activation energy) (Figure 3D, see SI for details). These results of the kinetic Monte Carlo simulation suggest that a distribution in the non-electrostatic contributions to desorption activation energy, which arise out of local defects and differences in the nanoscale chemical environment, may in fact dominate the kinetics of DNA desorption. Future PCV experiments, such as application of high-speed AFM, temperature and sweep rate dependence, should enable additional insights into the role of nanoscale heterogeneity in the orientational switching mechanism.

While we cannot treat the readsorptive ($\lambda < 0$, red) sweep as irreversible, we observe a significantly sharper transition from W* to A that likely originates from more uniform readsorption kinetics, which is plausible considering that the molecules in the W state, unlike those in state A which interact strongly with the surface, are expected to experience similar local interactions. The dispersion in the adsorption energy of A is likely to have only a minor influence on the activation energy because the transition state for the adsorption process likely resembles W more than it resembles A.

We then examined a surface decorated with thiolated 503 bp DNA on MCH. The longer DNA, expected to adhere to the surface more strongly than the 105 bp DNA, may provide additional insight into the interaction between the DNA and the SAM. At +200 mV, the average height of the protrusions, 3.6 nm, notably exceeds the diameter of a double-stranded DNA, suggesting that the 503mer is not parallel to the surface (Figure 5A,B). The stability of the protrusions suggests that the molecules are immobilized by strong interactions with the surface, probably in direct contact with gold at multiple points, producing segments tilting away from the surface and leading to heights exceeding 2.5 nm (Figure 5A). Applying a potential cyclically while imaging, we are able to reversibly switch the morphology of the protrusions (Figure 6). While the switching occurs at a similar potential range as the 105 bp DNA, we did not perform PCV analysis to compare the two molecular lengths as the analysis is complicated by many of the large protrusions containing multiple molecules. Notably, imaging the surface between successive series of potential sweeps revealed that the protrusions gradually converted to rods 1.5 nm high (Figures 5C–E, S10, and S11), which we did not observe with the shorter DNA. The average height suggests the molecules are in direct contact with gold (Table 1). DNA molecules

this long have significantly curved conformations when adsorbed on mica.[40] By contrast, the rods observed here are linear and exhibit a marked preference at discrete orientations 60° apart (Figure 5D inset). The transformation suggests that the 503mer, attracted by the surface charges, displaced the MCH molecules underneath and became embedded in the line defects of the SAM on Au(111), which are rotated by 60°.[69] The rods were shorter than the contour length of the 503 bp DNA and predominantly extended in only one of the two possible directions (Figure 7), indicating that the segments not strongly adsorbed were not observed, and displacement of the SAM likely initiated from one point (such as the tether) and propagated along the length. In contrast with the 105 bp DNA, the 503 bp DNA more readily induces larger SAM defects that allow it to be adsorbed on gold. Although the pressure exerted by DNA due to electrostatic attraction is estimated to be on the order of MPa, orders of magnitude (SI) below the GPa pressure required to displace an crystalline SAM,[70] the MCH SAM is known to be defective and mobile,[71] due to the weaker interchain interactions. The MCH molecules may then rearrange to accommodate the DNA. We do not expect the DNA is breaking the Au–S bond of the MCH molecules to release the thiolate, as it is energetically favored for MCH to diffuse laterally to accommodate the DNA so long as there are some vacancy defects in the SAM. In addition, repeated desorption of MCH due to DNA switching over the potential cycles would have resulted in a highly defective monolayer, which we did not observe. Drawn by strong electric fields from a transient defect, the DNA may displace the MCH molecules and enlarge the defect.

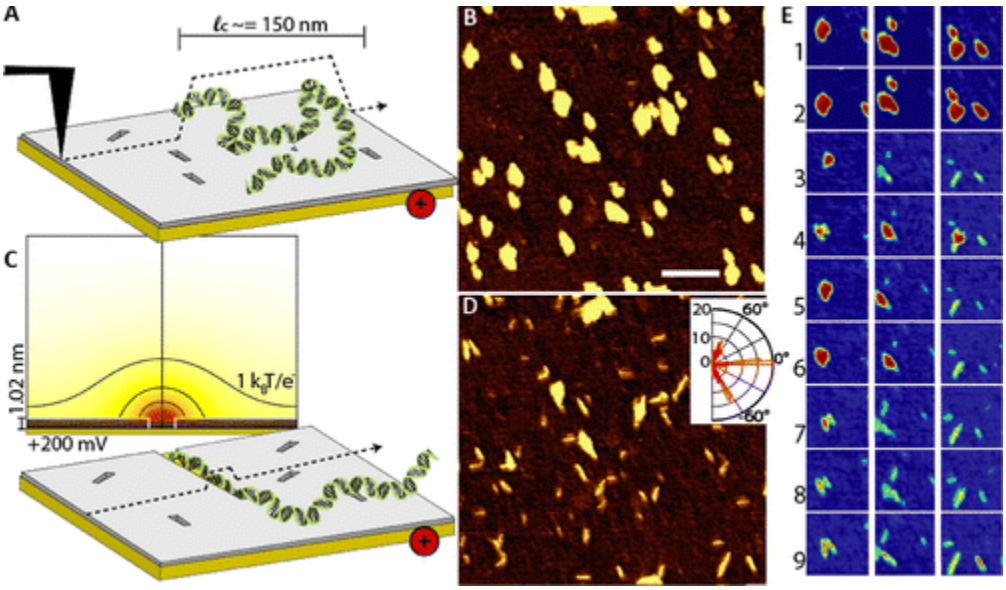

Figure 5. Evolution of thiolated 503bp DNA on MCH SAM after repeated cycles from +200 to −200 mV. (A) At positive potentials, the segments of the DNA may be trapped and some others may tilt away from the surface, producing features 3–4 nm tall above the background SAM. (B) Tapping-mode AFM image of long DNA (contour length $l_c \approx 150$ nm) at +200 mV. Scale bar is 100 nm. (C) After repeated potential cycling, the features at the same location become rod-like and the apparent height is reduced to 1.5 nm, suggesting that the DNA molecules are able to wedge themselves into local line defects within the monolayer. (Behind) Numerical solution of the modified Poisson–Boltzmann equation[57] for a 2.5 nm defect in a 6MH monolayer under 0.5×TAE. Each equipotential line represents 1 KbT/e (far away this voltage approaches zero) and the distribution shows stronger electric fields which attract the DNA into the defect site. The potential gradients are far greater than those above an ideal monolayer. (D) Topographical image

of DNA monolayer after several potential cycles. (Inset) Angular histogram of the orientation of the rod-like particles in D. (E) Three examples of 115 nm × 115 nm locations tracked and aligned[66] through consecutive (top to bottom) frames acquired between cycling of potentials. See SI for additional images and analysis.

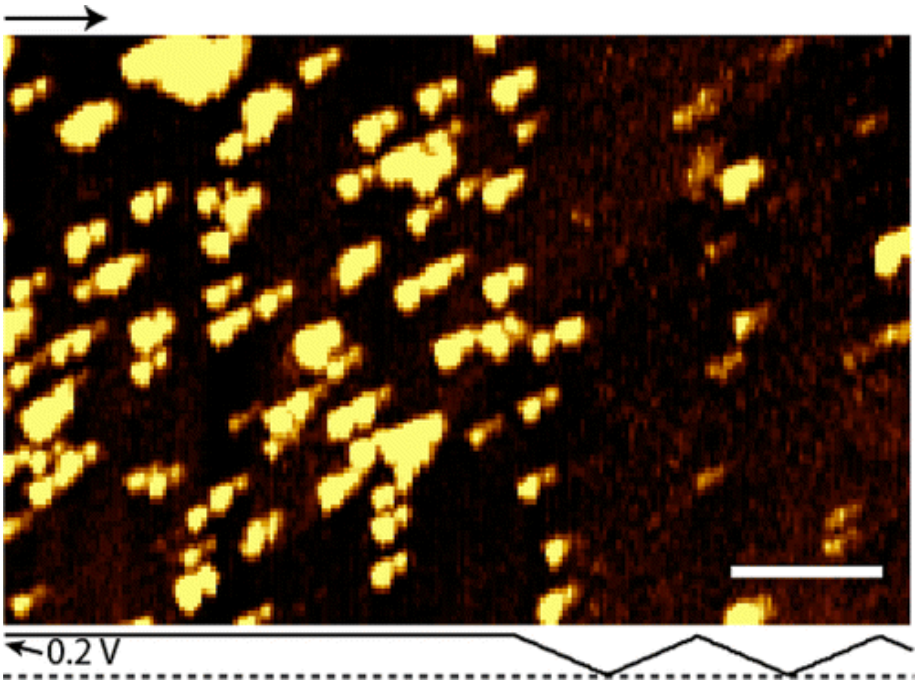

Figure 6. Reversible switching of 503 bp DNA on MCH. Prior to becoming embedded in the monolayer, the longer DNA was observed to undergo reversible morphology changes when subjected to cyclic applied potentials (below). We did not perform PCV analysis as many of the protrusions in fact contain multiple DNA molecules (as in Figure 5E). Scale bar is 100 nm.

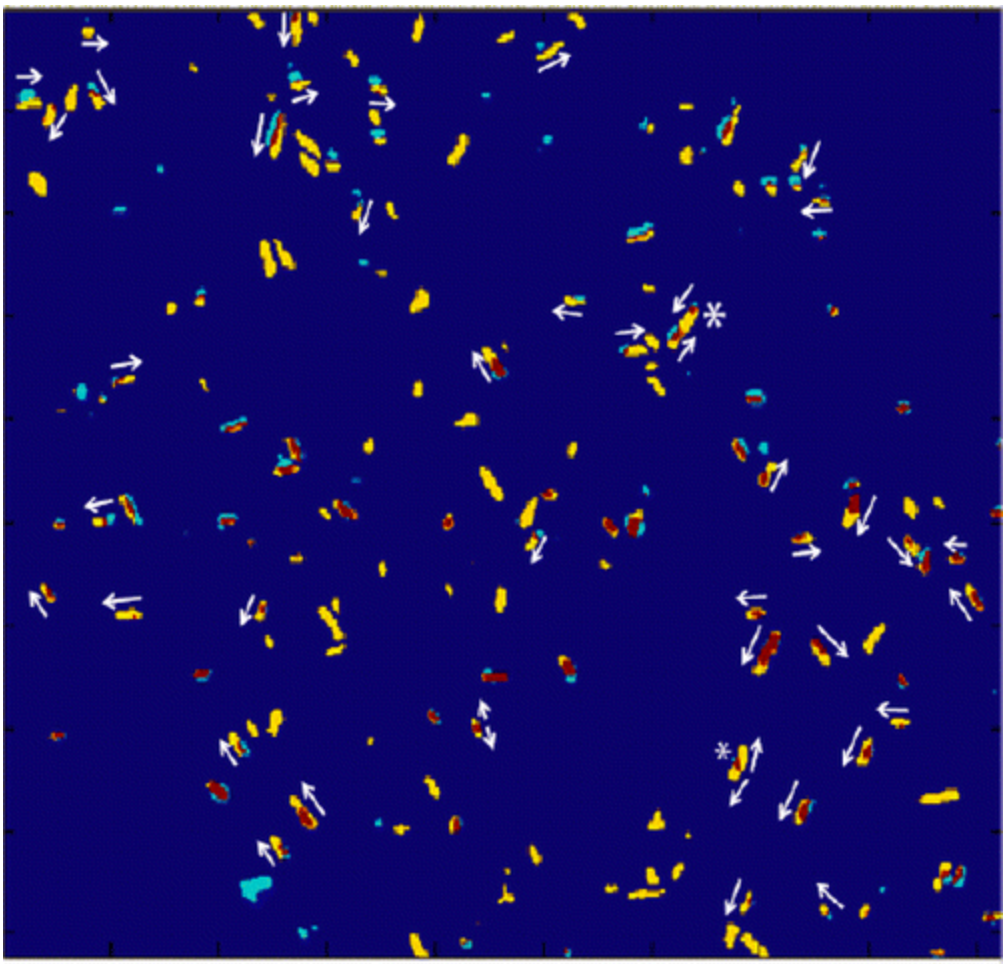

Figure 7. Aligned, overlaid frames of the locations of 503 bp DNA molecules in the middle of cycling sessions (Figure 5E-5) and after cycling sessions (Figure 5E-9) which demonstrate that extension of DNA mostly occurs in a single direction along the surface. Turquoise marks the location of DNA from the middle frame, yellow the location of the DNA features after cycling, red where the two overlap and dark blue is where no features were found. Arrows along the direction of growth were placed where growth in one direction could be unambiguously assigned. An asterisk was placed next to features showing convergent or divergent growth from smaller molecular features. Note that some intraframe drift prevents perfect alignment between the two images and shifts yellow features at the top of the frame in the down-right direction while those on the bottom are shifted in the up-left direction. Only DNA molecules which were located on the same level and were rod-like (not tall and rounded) were included in each frame.

Conclusion

By observing the dynamic switching of a biofunctional surface in operation, our study reveals the surprisingly prominent roles of the SAM defects on the conformation and dynamics of tethered DNA. These effects can be rationalized by stronger electric fields (Figure S8) and hydrophobic interactions in the defects. Compared to SAMs on our single-crystal substrate, the SAMs on the polycrystalline films, commonly used in DNA sensors, are more defective and the impact of defects on switching of tethered molecules may be even greater.[54] In static biosensors,

the denaturing of biomolecules due to adsorption on hydrophobic surfaces is a well-known cause of reduced sensitivity and device failure. Our study provides molecular scale evidence that precaution needs to be taken to avoid the displacement of the SAM which will deactivate DNA probes due to strong interaction with the substrate. Molecular-scale engineering of the surface chemistry[54] and intermolecular interactions[72-74] within the SAM should allow for more robust and dynamic biosensors; we are currently performing experiments to explore and quantify these effects using PCV analysis. On the other hand, controlling the interactions with tailored SAM defects may enable a stronger modulation of molecular properties in electrically switchable surfaces. Elucidating the effects of ionic strength and composition as well as the DNA sequence is likely to yield further control of these dynamic systems. Our study suggests that the switching of other molecules, such as charged proteins, on electrically switchable surfaces may be amenable to single-molecule techniques as well. Understanding of the conformations and dynamics of individual molecules on electrode surfaces will allow one to move beyond the existing models assuming identical biomolecules on inert, static monolayers and embrace the complexity of nanoscale systems in the development of surfaces capable of detecting low-copy-number biomolecules or introducing nanoscale perturbation to biological systems.

Supporting Information

Control experiments, additional potentiodynamic images of short DNA switching, explanation of kinetic Monte Carlo protocol, additional images of long DNA subjected to potential cycling, and estimations of electric fields and forces on the DNA. This material is available at https://doi.org/10.1021/ja3010946.

Acknowledgment

We acknowledge helpful discussions with Prof. Yanbao Ma and support from UC Merced. E.A.J. was supported by the UC Merced Faculty Mentor Fellowship.

References

1. Mendes, P. M. Chem. Soc. Rev. **2008**, 37, 2512– 2529 Google Scholar
2. Mrksich, M.; Yeo, W. S.; Yousaf, M. N. J. Am. Chem. Soc. **2003**, 125, 14994– 14995 Google Scholar
3. Rant, U.; Arinaga, K.; Scherer, S.; Pringsheim, E.; Fujita, S.; Yokoyama, N.; Tornow, M.; Abstreiter, G. Proc. Natl. Acad. Sci. U.S.A. **2007**, 104, 17364– 17369 Google Scholar
4. Rant, U.; Pringsheim, E.; Kaiser, W.; Arinaga, K.; Knezevic, J.; Tornow, M.; Fujita, S.; Yokoyama, N.; Abstreiter, G. Nano Lett. **2009**, 9, 1290– 1295 Google Scholar
5. Spuhler, P. S.; Knezevic, J.; Yalcin, A.; Bao, Q. Y.; Pringsheim, E.; Droge, P.; Rant, U.; Unlu, M. S. Proc. Natl. Acad. Sci. U.S.A. **2010**, 107, 1397– 1401 Google Scholar
6. Yeo, W. S.; Hodneland, C. D.; Mrksich, M. ChemBioChem **2001**, 2, 590– 593 Google Scholar

7. Kong, J. L.; Liu, Y.; Mu, L.; Liu, B. H.; Zhang, S.; Yang, P. Y. Chem. Commun. **2004**, 1194– 1195 Google Scholar

8. Kumar, A. S.; Ye, T.; Takami, T.; Yu, B. C.; Flatt, A. K.; Tour, J. M.; Weiss, P. S. Nano Lett. **2008**, 8, 1644– 1648 Google Scholar

9. Auernheimer, J.; Dahmen, C.; Hersel, U.; Bausch, A.; Kessler, H. J. Am. Chem. Soc. **2005**, 127, 16107– 16110 Google Scholar

10. Valiaev, A.; Abu-Lail, N. I.; Lim, D. W.; Chilkoti, A.; Zauscher, S. Langmuir **2007**, 23, 339– 344 Google Scholar

11. Frey, W.; Meyer, D. E.; Chilkoti, A. Adv. Mater. **2003**, 15, 248– 251 Google Scholar

12. Rant, U.; Arinaga, K.; Fujita, S.; Yokoyama, N.; Abstreiter, G.; Tornow, M. Org. Biomol. Chem. **2006**, 4, 3448– 3455 Google Scholar

13. Lahann, J.; Mitragotri, S.; Tran, T. N.; Kaido, H.; Sundaram, J.; Choi, I. S.; Hoffer, S.; Somorjai, G. A.; Langer, R. Science **2003**, 299, 371– 374 Google Scholar

14. Yeung, C. L.; Iqbal, P.; Allan, M.; Lashkor, M.; Preece, J. A.; Mendes, P. M. Adv. Funct. Mater. **2010**, 20, 2657– 2663 Google Scholar

15. Mertz, D.; Vogt, C.; Hemmerle, J.; Mutterer, J.; Ball, V.; Voegel, J. C.; Schaaf, P.; Lavalle, P. Nat. Mater. **2009**, 8, 731– 735 Google Scholar

16. Bard, A. J.; Faulkner, L. R. Electrochemical methods: fundamentals and applications; John Wiley: New York, 2001. Google Scholar

17. Rant, U.; Arinaga, K.; Fujita, S.; Yokoyama, N.; Abstreiter, G.; Tornow, M. Nano Lett. **2004**, 4, 2441– 2445 Google Scholar

18. Georgiadis, R. M.; Peterson, A. W.; Heaton, R. J. Nucleic Acids Res. **2001**, 29, 5163– 5168 Google Scholar

19. Heller, M. J.; Edman, C. F.; Raymond, D. E.; Wu, D. J.; Tu, E. G.; Sosnowski, R. G.; Butler, W. F.; Nerenberg, M. Nucleic Acids Res. **1997**, 25, 4907– 4914 Google Scholar

20. Steel, A. B.; Levicky, R. L.; Herne, T. M.; Tarlov, M. J. Biophys. J. **2000**, 79, 975– 981 Google Scholar

21. Ramirez, P.; Andreu, R.; Cuesta, A.; Calzado, C. J.; Calvente, J. J. Anal. Chem. **2007**, 79, 6473– 6479 Google Scholar

22. Fixe, F.; Branz, H. M.; Louro, N.; V, C.; Prazeres, D. M. F.; Conde, J. P. Nanotechnology **2005**, 16, 2061– 2071 Google Scholar

23. Georgiadis, R. M.; Heaton, R. J.; Peterson, A. W. Proc. Natl. Acad. Sci. U.S.A. **2001**, 98, 3701– 3704 Google Scholar

24. Melosh, N. A.; Wong, I. Y. Nano Lett. **2009**, 9, 3521– 3526 Google Scholar

25. Wong, I. Y.; Melosh, N. A. Biophys. J. **2010**, 98, 2954– 2963 Google Scholar

26. Sosnowski, R. G.; Tu, E.; Butler, W. F.; Oconnell, J. P.; Heller, M. J. Proc. Natl. Acad. Sci. U.S.A. **1997**, 94, 1119– 1123 Google Scholar

27. Mahajan, S.; Richardson, J.; Brown, T.; Bartlett, P. N. J. Am. Chem. Soc. **2008**, 130, 15589– 15601 Google Scholar

28. Mao, Y. D.; Liu, D. S.; Wang, S. T.; Luo, S. N.; Wang, W. X.; Yang, Y. L.; Qi, Q. Y.; Lei, J. Nucleic Acids Res. **2007**, 35, e33. DOI: http://dx.crossref.org/10.1093%2Fnar%2Fgkl1161 Google Scholar

29. Takeishi, S.; Rant, U.; Fujiwara, T.; Buchholz, K.; Usuki, T.; Arinaga, K.; Takemoto, K.; Yamaguchi, Y.; Tornow, M.; Fujita, S.; Abstreiter, G.; Yokoyama, N. J. Chem. Phys. **2004**, 120, 5501– 5504 Google Scholar

30. Murphy, J. N.; Cheng, A. K. H.; Yu, H. Z.; Bizzotto, D. J. Am. Chem. Soc. **2009**, 131, 4042– 4050 Google Scholar

31. Wang, K. M.; Yang, X. H.; Wang, Q.; Tan, W. H.; Yao, J.; Li, H. M. Langmuir **2006**, 22, 5654– 5659 Google Scholar

32. Herne, T. M.; Tarlov, M. J. J. Am. Chem. Soc. **1997**, 119, 8916– 8920 Google Scholar

33. Kaiser, W.; Rant, U. J. Am. Chem. Soc. **2010**, 132, 7935– 7945 Google Scholar

34. Lindsay, S. M.; Tao, N. J.; Derose, J. A.; Oden, P. I.; Lyubchenko, Y. L.; Harrington, R. E.; Shlyakhtenko, L. Biophys. J. **1992**, 61, 1570– 1584 Google Scholar

35. Zhang, Z. L.; Pang, D. W.; Zhang, R. Y.; Yan, J. W.; Mao, B. W.; Qi, Y. P. Bioconjugate Chem. **2002**, 13, 104– 109 Google Scholar

36. Ceres, D. M.; Barton, J. K. J. Am. Chem. Soc. **2003**, 125, 14964– 14965 Google Scholar

37. Barton, J. K.; Kelley, S. O.; Jackson, N. M.; McPherson, L. D.; Potter, A. B.; Spain, E. M.; Allen, M. J.; Hill, M. G. Langmuir **1998**, 14, 6781– 6784 Google Scholar

38. Erts, D.; Polyakov, B.; Olin, H.; Tuite, E. J. Phys. Chem. B **2003**, 107, 3591– 3597 Google Scholar

39. Hansma, H. G. Annu. Rev. Phys. Chem. **2001**, 52, 71– 92 Google Scholar

40. Hansma, H. G.; Revenko, I.; Kim, K.; Laney, D. E. Nucleic Acids Res. **1996**, 24, 713– 720 Google Scholar

41. Erdmann, M.; David, R.; Fornof, A.; Gaub, H. E. Nat. Nanotechnol. **2010**, 5, 154– 159 Google Scholar

42. Butt, H. J.; Cappella, B.; Kappl, M. Surf. Sci. Rep. **2005**, 59, 1– 152 Google Scholar

43. Clavilier, J.; Faure, R.; Guinet, G.; Durand, R. J. Electroanal. Chem. **1980**, 107, 205– 209 Google Scholar

44. Shuster, M. J.; Vaish, A.; Szapacs, M. E.; Anderson, M. E.; Weiss, P. S.; Andrews, A. M. Adv. Mater. **2008**, 20, 164 Google Scholar

45. Bumm, L. A.; Arnold, J. J.; Cygan, M. T.; Dunbar, T. D.; Burgin, T. P.; Jones, L.; Allara, D. L.; Tour, J. M.; Weiss, P. S. Science **1996**, 271, 1705– 1707 Google Scholar

46. Cygan, M. T.; Dunbar, T. D.; Arnold, J. J.; Bumm, L. A.; Shedlock, N. F.; Burgin, T. P.; Jones, L.; Allara, D. L.; Tour, J. M.; Weiss, P. S. J. Am. Chem. Soc. **1998**, 120, 2721– 2732 Google Scholar

47. Musgrove, A.; Kell, A.; Bizzotto, D. Langmuir **2008**, 24, 7881– 7888 Google Scholar

48. Springer handbook of experimental solid mechanics; Springer: Berlin, 2008. Google Scholar

49. Rant, U.; Arinaga, K.; Tornow, M.; Kim, Y. W.; Netz, R. R.; Fujita, S.; Yokoyama, N.; Abstreiter, G. Biophys. J. **2006**, 90, 3666– 3671 Google Scholar

50. Kolb, D. M.; Schneider, J. Electrochim. Acta **1986**, 31, 929– 936 Google Scholar

51. Yamada, R.; Uosaki, K. Langmuir **1998**, 14, 855– 861 Google Scholar

52. Maksymovych, P.; Sorescu, D. C.; Dougherty, D.; Yates, J. T. J. Phys. Chem. B **2005**, 109, 22463– 22468 Google Scholar

53. Tarek, M. Biophys. J. **2005**, 88, 4045– 4053 Google Scholar

54. Love, J. C.; Estroff, L. A.; Kriebel, J. K.; Nuzzo, R. G.; Whitesides, G. M. Chem. Rev. **2005**, 105, 1103– 1169 Google Scholar

55. Smith, C. P.; White, H. S. Langmuir **1993**, 9, 1– 3 Google Scholar

56. Israelachvili, J. N. Intermolecular and surface forces; Academic Press: San Diego, 1992. Google Scholar

57. Borukhov, I.; Andelman, D.; Orland, H. Phys. Rev. Lett. **1997**, 79, 435– 438 Google Scholar

58. Dzubiella, J.; Hansen, J. P. J. Chem. Phys. **2005**, 122, 234706. DOI: http://dx.doi.org/10.1063/1.1927514 Google Scholar

59. Ando, T.; Kodera, N.; Takai, E.; Maruyama, D.; Saito, K.; Toda, A. Proc. Natl. Acad. Sci. U.S.A. **2001**, 98, 12468– 12472 Google Scholar

60. Wickham, S. F. J.; Endo, M.; Katsuda, Y.; Hidaka, K.; Bath, J.; Sugiyama, H.; Turberfield, A. J. Nat. Nanotechnol. **2011**, 6, 166– 169 Google Scholar

61. Gillespie, D. T. JCoPh **1976**, 22, 403– 434 Google Scholar

62. Evans, E.; Ritchie, K. Biophys. J. **1997**, 72, 1541– 1555 Google Scholar

63. Bustamante, C.; Chemla, Y. R.; Forde, N. R.; Izhaky, D. Annu. Rev. Biochem. **2004**, 73, 705– 748 Google Scholar

64. Netz, R. R.; Joanny, J. F. Macromolecules **1999**, 32, 9013– 9025 Google Scholar

65. Friedsam, C.; Seitz, M.; Gaub, H. E. J. Phys.: Condens. Matter **2004**, 16, S2369– S2382 Google Scholar

66. Mantooth, B. A.; Donhauser, Z. J.; Kelly, K. F.; Weiss, P. S. Rev. Sci. Instrum. **2002**, 73, 313– 317 Google Scholar

67. Rowe, G. K.; Carter, M. T.; Richardson, J. N.; Murray, R. W. Langmuir **1995**, 11, 1797– 1806 Google Scholar

68. Patil, A. V.; Davis, J. J. J. Am. Chem. Soc. **2010**, 132, 16938– 16944 Google Scholar

69. Poirier, G. E.; Pylant, E. D.; White, J. M. J. Chem. Phys. **1996**, 105, 2089– 2092 Google Scholar

70. Liu, G. Y.; Salmeron, M. B. Langmuir **1994**, 10, 367– 370 Google Scholar

71. Poirier, G. E. Chem. Rev. **1997**, 97, 1117– 1127 Google Scholar

72. Lavrich, D. J.; Wetterer, S. M.; Bernasek, S. L.; Scoles, G. J. Phys. Chem. B **1998**, 102, 3456– 3465 Google Scholar

73. Lewis, P. A.; Smith, R. K.; Kelly, K. F.; Bumm, L. A.; Reed, S. M.; Clegg, R. S.; Gunderson, J. D.; Hutchison, J. E.; Weiss, P. S. J. Phys. Chem. B **2001**, 105, 10630– 10636 Google Scholar

74. Smith, R. K.; Reed, S. M.; Lewis, P. A.; Monnell, J. D.; Clegg, R. S.; Kelly, K. F.; Bumm, L. A.; Hutchison, J. E.; Weiss, P. S. J. Phys. Chem. B **2001**, 105, 1119– 1122 Google Scholar